

# The Solar Oxygen Abundance from an Empirical Three-Dimensional Model

H. Socas-Navarro<sup>1,2</sup>

<sup>1</sup> Instituto de Astrofísica de Canarias, Avda Vía Láctea S/N, La Laguna E-38200, Tenerife, Spain

<sup>2</sup> Departamento de Astrofísica, Universidad de La Laguna, 38205, La Laguna, Tenerife, Spain

## ABSTRACT

The Oxygen abundance in the solar photosphere, and consequently the solar metallicity itself, is still a controversial issue with far-reaching implications in many areas of Astrophysics. This paper presents a new determination obtained by fitting the forbidden O I line at 6300 Å with an *observational* 3D model. The approach presented here is novel because previous determinations were based either on 1D empirical stratifications or on 3D theoretical models. The resulting best-fit abundances are  $\log \epsilon(\text{O})=8.90$  and  $\log \epsilon(\text{Ni})=6.15$ . Nevertheless, introducing minor tweaks in the model and the procedure, it is possible to retrieve very different values, even down to  $\log \epsilon(\text{O})=8.70$ . This extreme sensitivity of the abundance to possible systematic effects is not something specific to this particular work but probably reflects the real uncertainty inherent to all abundance determinations based on a prescribed model atmosphere.

**Key words.** Sun: abundances – Sun: atmosphere – Sun: granulation – Sun: photosphere – Stars: abundances – Stars: atmospheres

## 1. Introduction

Oxygen is, after Hydrogen and Helium, the third most abundant element in the Universe. A precise knowledge of its abundance in stellar interiors is of critical importance in many areas of astrophysics because of its contribution to opacity, free electrons and also because it serves as a reference for other relevant elements that cannot be directly measured in the photospheric spectrum. Unfortunately, there are reasons to believe that our knowledge of even the solar oxygen abundance is still far from being precise. Several factors conspire to make it so elusive. First of all, Oxygen is a very volatile element and therefore its meteoritic abundance is not a valid proxy. Second, there are very few atomic indicators in the photospheric solar spectrum and they are all either extremely weak forbidden lines or complex transitions suffering of non-LTE effects and affected of additional uncertainties in the relevant atomic processes.

In spite of the uncertainties, the prevailing paradigm that emerged since the 1970s was that the solar Oxygen abundance was  $\log \epsilon(\text{O})$  in the range between 8.8 and 8.9, in the logarithmic scale commonly used in Astrophysics where H has a reference value of 12 (e.g., Cameron 1973; Anders & Grevesse 1989; Grevesse & Sauval 1998). In all cases, the procedure to determine chemical abundances was always the same: From a prescribed model atmosphere, one computes synthetic spectral lines and the abundances are adjusted until a satisfactory agreement is found with some atlas observations. The models employed were one-dimensional (1D), usually derived empirically by fitting a large number of lines and continua, and the photospheric observations were unresolved in space and time.

The paradigm was called under question by the controversial paper of Asplund et al. (2004) (hereafter AGSAK), claiming that the solar O abundance needed to be revised downwards by almost a factor of two ( $\log \epsilon(\text{O})=8.66$ ). The procedure was conceptually very similar to what had been done before except that, besides updated atomic parameters, the authors employed a three-dimensional (3D) model resulting from a hydrodynamical

numerical simulation. Obviously, such large revision would have a considerable impact on many areas of Astrophysics. In particular, it would ruin the excellent agreement existing between solar interior models and measurements from Helioseismology. Attempts to reconcile the models with the new abundances have been unsuccessful thus far (e.g., Basu & Antia 2008 and references therein; Basu & Antia 2013).

The debate on whether the proposed revision should be adopted has been very intense and several papers have been published with new abundance determinations, including those of Ayres et al. (2006); Socas-Navarro & Norton (2007); Ayres (2008); Centeno & Socas-Navarro (2008); Caffau et al. (2008); Scott et al. (2009); Pereira et al. (2009); Caffau et al. (2011). The frequency of publications on the so-called *solar oxygen crisis* seems to have declined in recent years, not because the issue has been satisfactorily resolved but probably because there are no new arguments or data in favor of one view or the other. Whatever the final outcome is, the work of AGSAK has been of great importance because, at the very least, it has blown the whistle on a grossly overlooked problem, namely how much can we trust our abundance determinations. The choice of a suitable atmospheric model is critical and it is not yet clear what the model uncertainties are or how those uncertainties propagate into the final result. Ayres (2008) correctly remarks that, while a 3D atmosphere is preferable over a 1D, it is not clear that a model resulting from a numerical simulation is better than an empirical one when it is employed to fit observations. In addition, the work of Caffau et al. (2008, 2011) demonstrates that going to 3D does not necessarily result in lower abundances.

The present paper is an attempt to resolve the dilemma of theoretical 3D versus empirical 1D by taking the best of both approaches. A 3D model obtained from observations is used to derive the O and Ni abundances in the conventional way (i.e., fitting unresolved atlas observations). As in my previous works on this subject (Socas-Navarro & Norton 2007; Centeno & Socas-Navarro 2008), the focus is not so much the final result but the introduction of a novel methodology, hoping

that it might open a new path for better, more robust determinations in the future.

## 2. Observations and the model

The 3D model was derived from a reanalysis of the data used in Socas-Navarro (2011, hereafter SN11) with a slightly different approach and a new version of the code NICOLE (Socas-Navarro et al. 2014). The new version incorporates several improvements in accuracy and stability that make the model smoother and with a lower *inversion noise* (the pixel-to-pixel fluctuation exhibited by the retrieved parameters, such as the photospheric temperature). Some other improvements include:

- The new NICOLE version supports 2-component inversions. Pixels that exhibit polarization signal above a certain threshold (32% of the total) are inverted here with a full 2-component treatment, which is more consistent than the approach taken in the SN11 paper.
- A regularization term is added to the  $\chi^2$  merit function to favor (when possible) smoother solutions over those with spurious high-frequency vertical fluctuations.
- A Bezier spline interpolation scheme is now used to reconstruct the model atmosphere from the node values. Previously, the model was constructed from linear segments between the nodes. The new scheme results in smoother height runs of the retrieved physical parameters, thus getting rid of unsightly sharp corners and at the same time minimizing the possibility of overshooting between the nodes. For stability reasons, it is important to keep the model within reasonable ranges of the various physical parameters at every step of the iterative procedure. The algorithm sets constraints on the node values but the interpolation between nodes might overshoot beyond the safe range. This risk is minimized by the use of Bezier interpolation, which behaves similarly to splines with tension.
- Includes hyperfine structure arising from the angular momentum coupling between electron and nuclear spin.

The dataset from which the model has been derived is exactly the same as in SN11. A brief description is provided here for a sake of completeness but the reader is referred to that paper for more details. The data come from the Spectro-Polarimeter (SP) of the Hinode satellite’s Solar Optical Telescope (SOT; Kosugi et al. 2007; Ichimoto et al. 2008; Shimizu et al. 2008; Suematsu et al. 2008; Tsuneta et al. 2008), particularly from a quiet Sun observation acquired at UT 19:32:10 on 2007 September 24.

The SP scan spans the wavelength range between 6300.89 and 6303.29 Å with a sampling of 21.4 mÅ. Unfortunately the O/Ni blend at 6300.27 Å that is the target of this study is just outside the observed range. It is therefore impossible to perform here a pixel-by-pixel abundance analysis *a la* Socas-Navarro & Norton (2007), which would be of great interest e.g., to gauge with high confidence and precision the total error of the entire procedure. Instead, element abundances are derived here by fitting the disk-center average intensity from the Kitt Peak Fourier Transform Spectrometer (FTS) atlas of Neckel & Labs (1984), following the traditional procedure of synthesizing line profiles from the model and taking the spatial average of the synthetic spectra to compare with the atlas. Absolute wavelengths were obtained by comparing the average observed spectrum to the FTS atlas. The spectral point spread function of the Hinode SP is known and has been considered

in the analysis by applying it on the emergent synthetic spectra. This means that, at each iterative step, the synthetic profiles produced by the proposed model are convolved with the Hinode PSF before being compared to the observed ones.

The field of view observed by the Hinode SOT is a very quiet region at disk center. Spatial sampling is about 0.15”, which is approximately half of the actual spatial resolution given by the SOT point spread function. Standard flatfielding and polarimetric calibration procedures were applied to the spectra. Some other corrections were applied *a posteriori* as detailed in SN11.

The inversion fits both Fe I lines at 6301.5 Å and 6302.5 Å simultaneously. There are some small departure from LTE (Shchukina & Trujillo Bueno 2001) which are taken into account in the procedure using the approximation described in SN11. Three different inversions were carried out varying the assumed Fe abundance (7.40, 7.45 and 7.50, respectively), resulting in three slightly different 3D models. This will be helpful to gauge the influence of our uncertainties in the model on the abundances obtained. The atomic line data employed are listed in Table 1. They are mostly those resulting from a query to the VALD database (Piskunov et al. 1995; Kupka et al. 1999; Kupka et al. 2000), with the following remarks. The oscillator strength for Fe I 6301.5 is from Bard et al. (1991). In the absence of actual laboratory data for the 6302.5 line, the  $\log(gf)$  derived empirically by SN11 is used here. For both Fe I lines, collisional broadening is treated using the method of Anstee & O’Mara (1995). The broadening constants, listed in Table 1, are obtained with the code of Barklem et al. (1998). The wavelength correction (20 mÅ to the blue) applied to the Sc II line by Ayres (2008) is necessary here, as well. For the  $\log(gf)$ , however, no further adjustment was needed. The original line strength from the VALD database combined with the meteoritic Sc abundance yields a satisfactory fit to the line shape, as shown below. Oscillator strengths for the two relevant Ni isotopes (treated here as two blended lines with a slight wavelength shift) are from Johansson et al. (2003). Finally, for the forbidden O I line, the value adopted is that from Storey & Zeippen (2000), as recommended by Scott et al. (2009).

As noted above, the inversion is done differently depending on whether the spatial pixel to invert is magnetic or not. Magnetic pixels are defined as those that exhibit polarization signal above the  $3 - \sigma$  noise level in any one of the Stokes profiles  $Q$ ,  $U$  or  $V$ . In both cases the model is initialized with the HSRA as starting guess (Gingerich et al. 1971) and then iterated in two successive cycles. The number of nodes used in the inversions for the various physical parameters is listed in Table 2. Note that the inversion corresponding to the second cycle of magnetic pixels uses a 2-component model and it has a different number of nodes for each component. In those cases (magnetic pixels), the atmosphere is parameterized as consisting of a magnetic component (Comp 2 in the table) coexisting with some filling factor inside the pixel with a non-magnetic surrounding (Comp 1).

Some representative fits are shown in Figure 1 to give an idea of how accurately the synthetic lines match the observations. Perhaps the most relevant plot for the discussion here is the top-left panel, which shows the spatially-averaged profiles. Notice that this is not actually a fit but the result of combining all the individual synthetic profiles together and comparing it to the average of the observations. The other three panels show typical fits in magnetic and non-magnetic pixels.

Figure 2 illustrates the spatial distribution of some sample quantities. No effort has been made to put the model on a common geometrical scale since that is irrelevant for the pur-

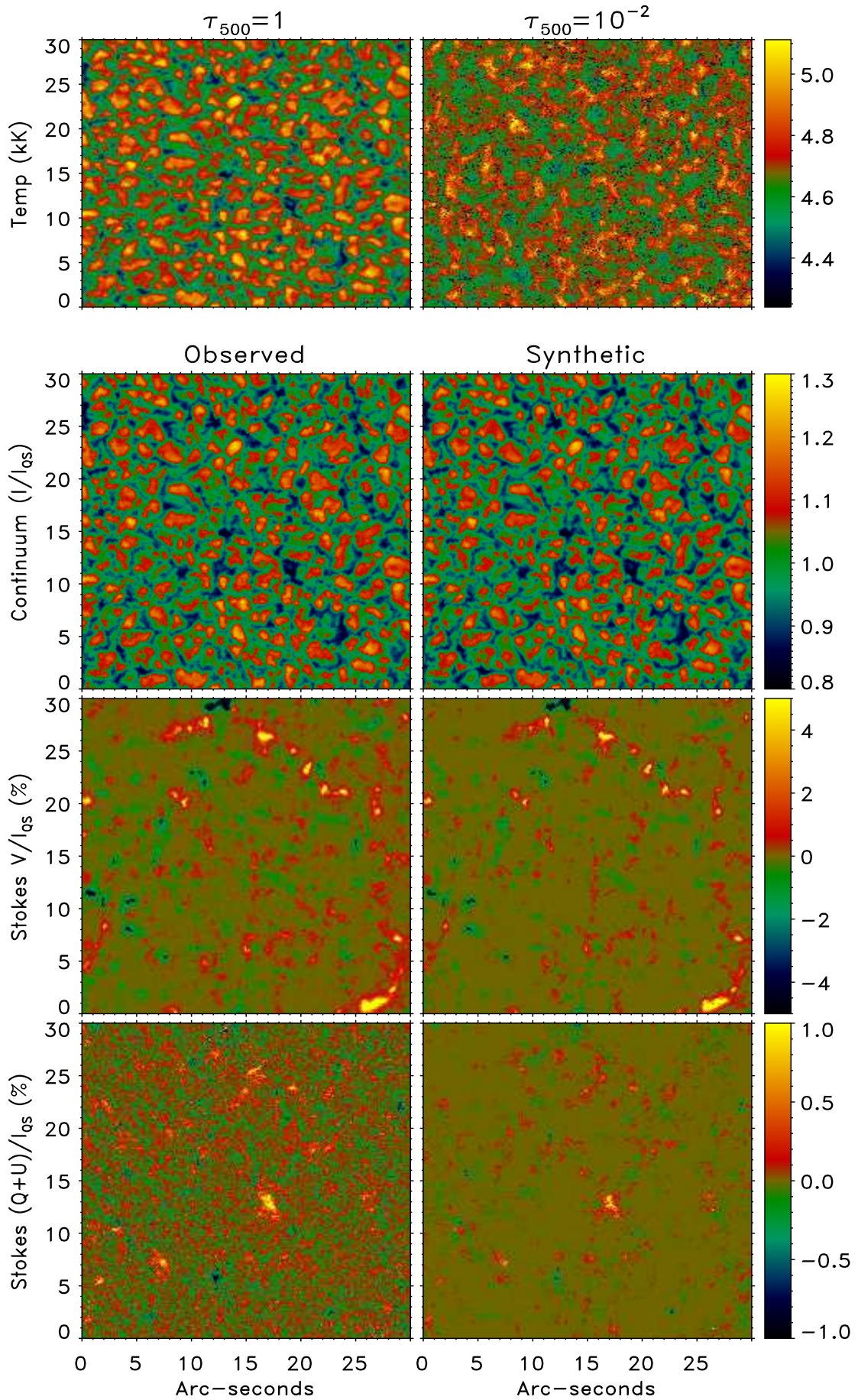


**Fig. 2.** Spatial distribution of various magnitudes derived from the empirical 3D model used in this work. Top panels: Horizontal cuts of the temperature at the base of the photosphere (left) and at the height where  $\log(\tau_{500}) = 10^{-2}$  (right). The rest of the panels show a comparison between various observed (left) and synthetic (right) quantities.

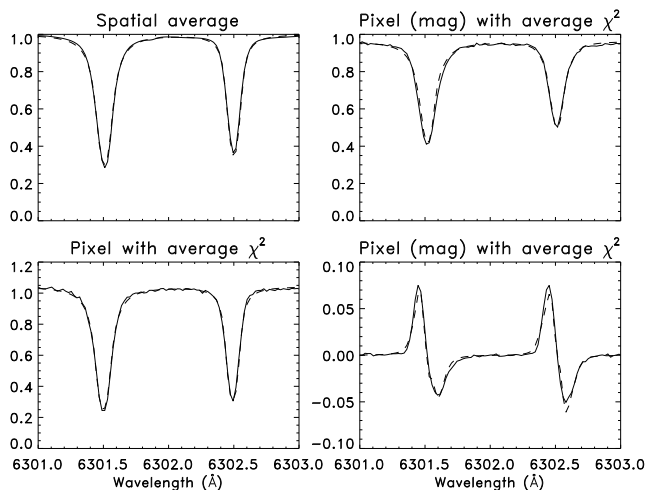


**Fig. 1.** Some representative fits obtained with the empirical 3D model. In all panels the solid line is the Hinode observations and the dashed line is the synthetic profile computed with NICOLE. Upper left: Spatial average over the entire field of view. Lower left: Fit to a non-magnetic profile whose  $\chi^2$  is similar to the average  $\chi^2$  in all the non-magnetic pixels. The quality of this fit may then be considered as typical of the entire region. Right panels: Fits to Stokes  $I$  (upper) and  $V$  (lower) profiles from a pixel with magnetic signal whose  $\chi^2$  is similar to the average  $\chi^2$  in all the magnetic pixels. The quality of this fit may then be considered as typical of the entire region.

pose of computing the emerging profile from each model column. Therefore, the reference height scale employed in this paper is the monochromatic continuum optical depth at 500 nm,  $\log(\tau_{500})$ .

As with the earlier version, the new 3D model is publicly available and may be downloaded from:

`ftp://download:data@ftp.iac.es/`

The files are licensed under the GPLv3 general public license<sup>1</sup> which explicitly grants permission to copy, modify (with proper credit to the original source and explanation of the modifications) and redistribute it.

### 3. Analysis

#### 3.1. The Sc II line and the missing dynamics

Very close to the O/Ni blend that constitutes the main target of this study lies another interesting spectral feature of similarly weak nature, emerging from a Sc II transition. This line is of great interest for reasons that shall be explained below and has been included in the synthetic spectrum computed from the 3D model. In order to calculate the Sc II profile one needs to consider its hyperfine structure. Fortunately, accurate atomic parameters exist in the literature (e.g., in the VALD database) and one can easily feed those values into NICOLE to produce realistic line shapes.

The inclusion of hyperfine structure for the Sc II line slows down the calculation by nearly a factor 100. As a result, computing the  $200 \times 200$  columns of the 3D model takes a significant (but still feasible) amount of time. However, it quickly becomes prohibitive to repeat the full model synthesis for each point in the three-parameter grid of abundances of Fe, Ni and O required for

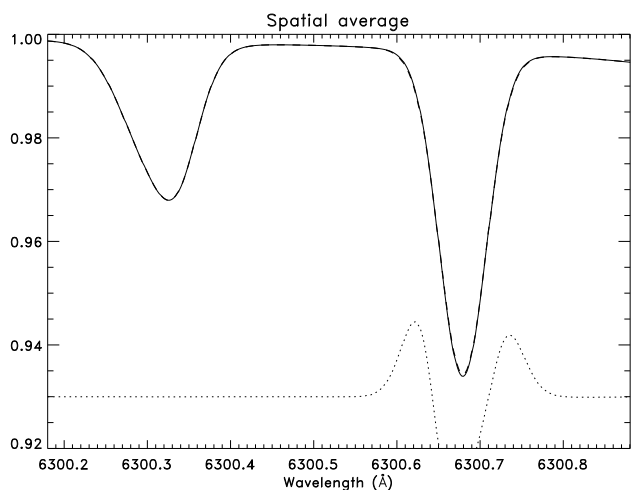


**Fig. 3.** Comparison of hyperfine splitting effects (solid) and an *ad hoc* broadening (dashed) of  $0.8 \text{ km s}^{-1}$  on the average profile of the Sc II spectral line. The dotted line shows the difference between both profiles, multiplied by a factor 50 and conveniently offset for the sake of easy visualization.

the abundance determination in Sect 4 below. It is then convenient, if not entirely necessary, to find computationally cheaper alternatives.

The overall effect of the hyperfine structure on the *spatially averaged* Sc II intensity profile is simply a broadening of the line. With some experimentation, it is straightforward to see that the average Sc II synthetic profile emerging from the 3D model is nearly identical to one computed without hyperfine structure but adding a microturbulent velocity of  $0.8 \text{ km s}^{-1}$ , as seen in Fig (3). The extra parameters, in addition to those in Table 1, needed for the hyperfine structure calculation (Young et al. 1988; Arnesen et al. 1982) are:  $I=3.5$ ,  $A_{low}=-27.9$ ,  $B_{low}=19$ ,  $A_{up}=125.4$ ,  $B_{up}=7$ , with all A and B constants in MHz. In view of this result, all the calculations shown in the remainder of this paper have been carried out simulating the effects of hyperfine structure in the Sc II line by applying an “artificial” microturbulence of  $0.8 \text{ km s}^{-1}$  (only to this line!), which is a very good approximation for the spatially averaged intensity.

A first comparison of the synthetic spectrum to the atlas observation, plotted in Fig (4), shows that it is possible to reach a reasonable agreement in the O/Ni blend but a very poor fit to the Sc II line. The abundance values for the calculation in the figure are  $\log \epsilon(\text{Fe})=7.50$ ,  $\log \epsilon(\text{O})=8.80$ ,  $\log \epsilon(\text{Ni})=6.20$ . The discrepancy of the Sc II feature is too large to be reconciled by tweaking its abundance or the atomic parameters. It is possible to make the line core deeper by increasing its abundance or oscillator strength but it would still be too narrow compared to the observed profile.

In order to bring the synthetic Sc II line into agreement with the observation, it is necessary to add some additional broadening. The natural explanation for the missing broadening is to assume that, even with Hinode’s high spatial resolution, there are still some small-scale plasma flows at the base of the photosphere that are not being sufficiently resolved in the observations. It is important to note that the Fe I lines are very well reproduced without requiring any microturbulence, which indicates that most of the small-scale dynamics seen by these lines has been properly captured in the 3D model. Therefore, the missing dynamics is probably located in the deeper layers, where the

<sup>1</sup> See <http://www.gnu.org/licenses/gpl.html>

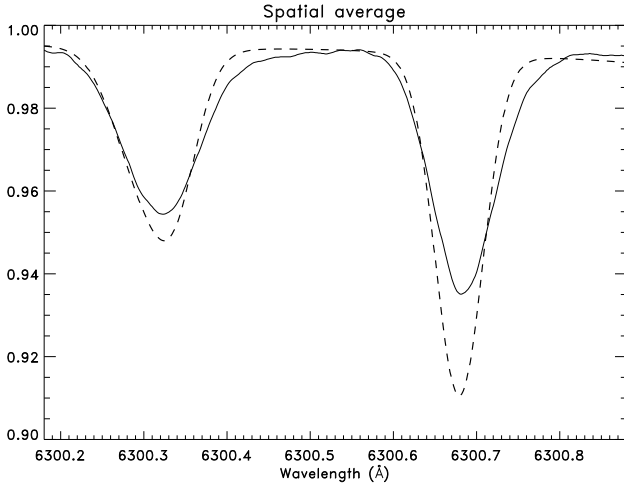


**Fig. 4.** The synthetic Sc II line at 6300.68 Å (dashed) is too narrow when compared to the observed atlas (solid) for any combination of abundance and oscillator strength.

O/Ni and the Sc II lines form but the Fe I lines have very little sensitivity.

A comparison of the 3D model employed here with the hydrodynamical simulation of AGSAK further supports the notion of the missing dynamics scenario. The *rms* spread of velocities at the  $\log(\tau_{500}) = 1$  level is much larger in the simulation than in the 3D empirical model. With the information provided by the Sc II line, it is straightforward to correct this problem by applying an *ad-hoc* enhancement factor  $v_{enh}$  to the velocities in the model and tweaking this factor until the line is properly fitted. Since the Sc II line has a very similar strength and formation region to the O/Ni blend, this enhancement will also correct any possible missing broadening in the O and Ni features. After some experimentation, it was found that the optimal *rms* spread for the Sc II line is  $v_{rms} = 1.36 \text{ km s}^{-1}$ , about a factor of 2 greater than in the empirical model. This figure is considerably lower than the  $2.47 \text{ km s}^{-1}$  of the AGSAK model. In fact, adopting their value of the *rms* velocity spread would result in *excessive* broadening of the observed Sc II line, incompatible with the observations. With the correction described here, the agreement between observed and average synthetic profiles improves enormously, as shown below.

#### 4. Abundance determinations

Having a 3D model that accurately reproduces the Sc II line, we can now proceed with confidence to the derivation of the O and Ni abundance by the usual procedure. One computes the synthetic profiles of the O/Ni blend for an array of  $[\log \epsilon(\text{O}), \log \epsilon(\text{Ni})]$  values at each model column, takes the spatial average over the entire field of view and compares the result to the observation in order to find which pair of abundances produces the best match. The comparison is performed by defining, for each set of abundances, a  $\chi^2$  function as the sum of the quadratic difference between synthetic and observed profiles for all wavelengths in the range.

Since there are actually three slightly different 3D models, resulting from using three different Fe abundances ( $\log \epsilon(\text{Fe}) = 7.40, 7.45$  and  $7.50$ ) in the inversion of the Hinode Fe I profiles, we perform the comparison for all three cases, resulting in an effective three-dimensional grid of abundances

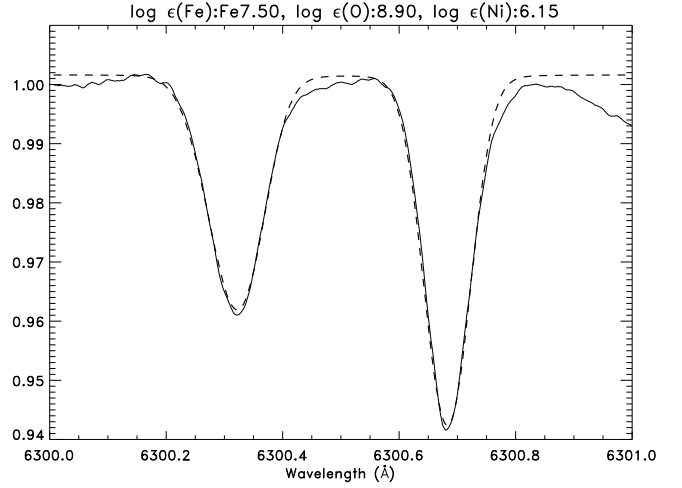


**Fig. 5.** Best fit to the [O/Ni] feature in the abundance grid.

( $\log \epsilon(\text{Fe}), \log \epsilon(\text{O}), \log \epsilon(\text{Ni})$ ). Even though the best value for the solar Fe abundance is probably  $\log \epsilon(\text{Fe}) = 7.50$ , as concluded by previous works (Shchukina & Trujillo Bueno 2001), it is nevertheless interesting to use the three inversion results as this will hopefully provide some insight into how slight changes in the model can influence the inferred abundances.

The profiles plotted in Fig 5 represent the best fit. The corresponding triplet of abundance values is  $\log \epsilon(\text{Fe}) = 7.50$ ,  $\log \epsilon(\text{O}) = 8.90$  and  $\log \epsilon(\text{Ni}) = 6.15$ . As a side note, the Sc abundance required to fit this line is the meteoritic value of 3.05.

To illustrate how the fit degrades as one moves away from the optimal set of abundances, Fig 6 shows the second best fit in the grid. This new fit was obtained with  $\log \epsilon(\text{O}) = 8.95$  and  $\log \epsilon(\text{Ni}) = 6.10$  and the resulting  $\chi^2$  is only 20% higher than before. We can see in the figure that that fit is remarkably tight, even though the difference in O abundance is rather significant. A comparison of the results obtained with all three models (corresponding to  $\log \epsilon(\text{Fe}) = 7.40, 7.45$  and  $7.50$ ) shows that the best fit is always achieved with  $\log \epsilon(\text{O}) = 8.90$  and  $\log \epsilon(\text{Ni})$  varying between 6.10 and 6.15, in all three cases with similarly good fits to those shown in Fig 5. If we also include the second best match in the comparison, we have three more values to consider. As before, the  $\chi^2$  is only slightly worse than for the best (30% higher, at the most) and the fits look visually very similar to those in Fig 5. In this case, the spread of good fit abundances increases to the range from 8.85 to 8.95 for  $\log \epsilon(\text{O})$  and remains between 6.10 and 6.15 for  $\log \epsilon(\text{Ni})$ .

In order to further explore the sensitivity of the abundance results to the model employed for the calculation, the same procedure was applied to a slightly perturbed version of the  $\log \epsilon(\text{Fe}) = 7.50$  model. The perturbation consists of a linear addition to the temperature in the range of optical depths  $\log(\tau_{500}) = (-1, 1)$  and has a total amplitude of 50 K, going from +25 K at  $\log(\tau_{500}) = 1$  down to -25 K at  $\log(\tau_{500}) = -1$ . With such small perturbation, the inferred abundances of O and Ni change to 8.95 and 6.10, respectively.

Other factors that affect the result are the continuum reference and the wavelength calibration. If the continuum is chosen slightly lower or higher, both O and Ni abundances will change accordingly. This is a common problem in all abundance determinations. Similarly, a slight wavelength shift of a few mÅ might be compensated by altering the ratio of O and Ni in the blend to recover a good fit. Finally, the line broadening produced

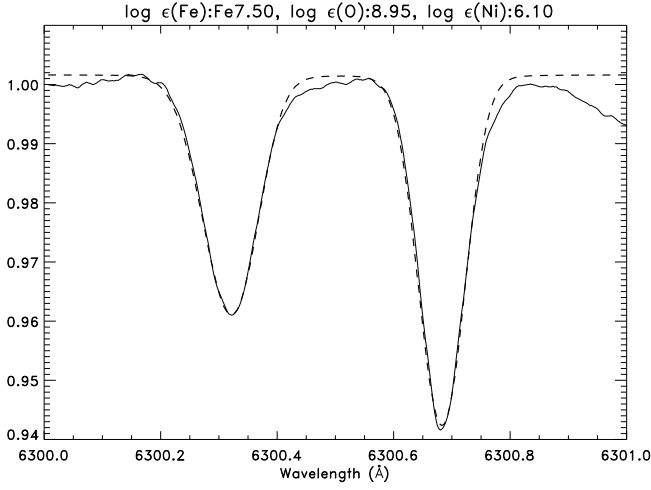


**Fig. 6.** Second best fit to the [O/Ni] feature in the abundance grid.

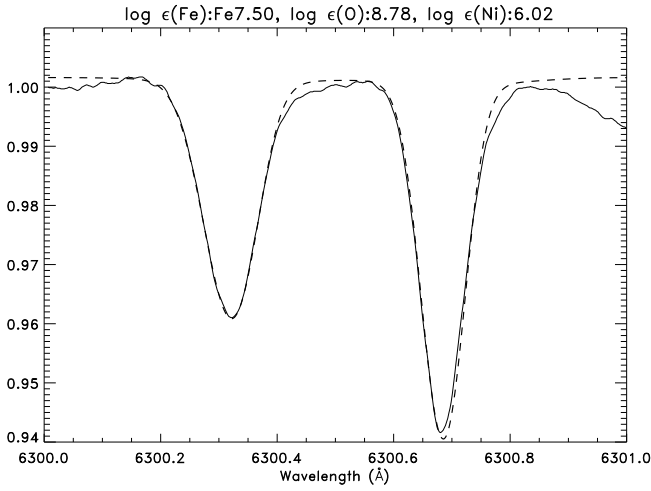


**Fig. 7.** Best fit abundances using a slightly perturbed model with a perturbation in temperature ranging from 50 K at  $\log(\tau_{500})=1$  to -50 K at  $\log(\tau_{500})=-1$ .

by the dynamics going on in the lower photosphere has a significant impact, as well. The AGSAK dynamics is incompatible with the Sc II line but still, even slight changes in the adopted *rms* velocity will have an impact on the result.

Playing with all of the above factors, it is even possible to achieve an O abundance compatible with that of AGSAK. The actual fit is shown in Fig 8. Notice how the fit is still remarkably good, given how discrepant these new abundances are compared to the previous figures, which again illustrates how extremely sensitive these results are to small details of the model or of the procedure in general. In order to produce this low abundance, the velocity enhancement at the base of the photosphere was reduced by a 15% (bringing the *rms* velocity at that layer down from 1.36 to 1.15 km s<sup>-1</sup>), the wavelength scale was shifted 2 mÅ and the continuum reference was decreased by 10<sup>-3</sup>. The Sc II line became slightly narrower and deeper with the change in the model, creating a very noticeable discrepancy at the line core. This was compensated by decreasing its abundance/ $\log(gf)$  by 6%. In this manner, the fit to the Sc II line is slightly worse than it was before but, as Fig 8 shows, it might still be considered acceptable.

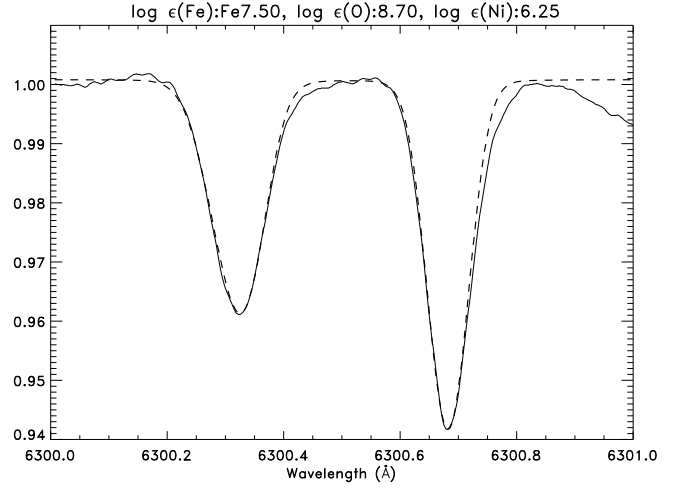


**Fig. 8.** Fits with a low O abundance obtained after minor tweaks to the model atmosphere and the continuum reference selection. The goodness of this fit illustrates the high sensitivity of abundance determinations to the particular details of the model or the procedure.

## 5. Discussion

This paper presents a novel approach to the O abundance determination using a 3D model that has been obtained from observations, as opposed to most recent works that use a hydrodynamical simulation. Since the model is obtained by inverting the much stronger Fe I lines at 6301.5 and 6302.5 Å observed by the Hinode SP, it seems to be missing some of the dynamics that take place in the deeper formation region of the O/Ni blend. This could be due to a lack of spatial resolution or to the weak sensitivity of the stronger Fe I lines to plasma motions in a layer very close to the continuum formation region. Ayres (2008) already gave a hint that this could be a problem and noted, with remarkable perspicacity, that “a possible disadvantage is that the derived motions will depend on the instrumental resolution and might not be as vigorous as in fully resolved 3D theoretical models”. Fortunately, this issue can be overcome by using the nearby Sc II line, which is of very similar strength to the O/Ni blend and probes the same atmospheric region.

In principle, the results obtained are in the high range ( $\log \epsilon(\text{O})=8.9 \pm 0.1$ ), compatible with the “old” solar composition. However, in view of how sensitive the results are to the details of the model atmosphere (it is even possible to produce values compatible with the “new” composition with very minor tweaks), I believe they should be taken with some reservation. In fact, the same caution should probably be adopted with all previous results on abundance determinations based on the traditional technique of fitting atlas observations with a prescribed model atmosphere. Ultimately, the reliability of our abundances is limited by the uncertainty in the models employed, of which we still lack such detailed understanding. It is then almost impossible to ascribe meaningful error bars to those measurements. A thorough study of the systematic errors arising from the use of a prescribed model and other parameters employed in the abundance analysis is urgently needed in order to gain a better understanding of our limitations.

An important conclusion to draw from this study is that one does not necessarily obtain the “low” O abundance of AGSAK ( $\log \epsilon(\text{O})=8.66$ ) when using a 3D model with recent atomic data. Intermediate (Caffau et al. 2008) and high (this work) abun-

dances may be obtained from 3D models, as well. Furthermore, given the sensitivity of the results to the details of the analysis, we should also question to what degree an analysis based on equivalent widths (which is what has been employed in most cases thus far) is enough to capture all the subtleties that are observed in a detailed fit. It seems that in difficult situations, such as this one, it is necessary to work with a full line analysis quantified by some merit function (e.g., the  $\chi^2$  used here).

In the solar case there is an obvious way to improve the overall procedure and increase our confidence in the measurement of element abundances. Using spatially-resolved observations, it is possible to conduct a pixel-by-pixel analysis, similarly to how it was done in Socas-Navarro & Norton (2007). If one has systematic errors, there is no reason to expect that all of the analyzed spectra will yield consistent results. Therefore, the pixel-to-pixel distribution is a perfect sanity check to diagnose possible systematic errors. In that paper we found a fluctuating pattern of abundances, correlated with the granulation distribution. This inconsistency was probably a reflection of the uncertainties in the non-LTE line formation physics. Conducting a similar study with simpler lines such as the forbidden transition analyzed here would undoubtedly cast some more light into this important issue.

*Acknowledgements.* Hinode is a Japanese mission developed and launched by ISAS/JAXA, collaborating with NAOJ as a domestic partner, NASA and STFC (UK) as international partners. Scientific operation of the Hinode mission is conducted by the Hinode science team organized at ISAS/JAXA. This team mainly consists of scientists from institutes in the partner countries. Support for the post-launch operation is provided by JAXA and NAOJ (Japan), STFC (U.K.), NASA, ESA, and NSC (Norway).

The author thankfully acknowledges the technical expertise and assistance provided by the Spanish Supercomputing Network (Red Española de Supercomputación), as well as the computer resources used: the LaPalma Supercomputer, located at the Instituto de Astrofísica de Canarias.

Financial support by the Spanish Ministry of Science and Innovation through project AYA2010-18029 (Solar Magnetism and Astrophysical Spectropolarimetry) is gratefully acknowledged.

The VALD database (referenced in the text) was used to obtain atomic parameters for the Sc II line.

## References

- Anders, E. & Grevesse, N. 1989, *Geochim. Cosmochim. Acta*, 53, 197
- Anstee, S. D. & O'Mara, B. J. 1995, *MNRAS*, 276, 859
- Arnesen, A., Hallin, R., Nordling, C., et al. 1982, *A&A*, 106, 327
- Asplund, M., Grevesse, N., Sauval, A. J., Allende Prieto, C., & Kiselman, D. 2004, *A&A*, 417, 751
- Ayres, T. R. 2008, *ApJ*, 686, 731
- Ayres, T. R., Plymate, C., & Keller, C. U. 2006, *ApJS*, 165, 618
- Bard, A., Kock, A., & Kock, M. 1991, *A&A*, 248, 315
- Barklem, P. S., Anstee, S. D., & O'Mara, B. J. 1998, *PASA*, 15, 336
- Basu, S. & Antia, H. M. 2008, *Phys. Rep.*, 457, 217
- Basu, S. & Antia, H. M. 2013, *Journal of Physics Conference Series*, 440, 012017
- Caffau, E., Ludwig, H., Steffen, M., et al. 2008, *A&A*, 488, 1031
- Caffau, E., Ludwig, H.-G., Steffen, M., Freytag, B., & Bonifacio, P. 2011, *Sol. Phys.*, 268, 255
- Cameron, A. G. W. 1973, *Space Sci. Rev.*, 15, 121
- Centeno, R. & Socas-Navarro, H. 2008, *ApJ*, 682, L61
- Gingerich, O., Noyes, R. W., Kalkofen, W., & Cuny, Y. 1971, *Sol. Phys.*, 18, 347
- Grevesse, N. & Sauval, A. J. 1998, *Space Science Reviews*, 85, 161
- Ichimoto, K., Lites, B., Elmore, D., et al. 2008, *Sol. Phys.*, 249, 233
- Johansson, S., Litzén, U., Lundberg, H., & Zhang, Z. 2003, *ApJ*, 584, L107
- Kosugi, T., Matsuzaki, K., Sakao, T., et al. 2007, *Sol. Phys.*, 243, 3
- Kupka, F., Piskunov, N., Ryabchikova, T. A., Stempels, H. C., & Weiss, W. W. 1999, *A&AS*, 138, 119
- Kupka, F. G., Ryabchikova, T. A., Piskunov, N. E., Stempels, H. C., & Weiss, W. W. 2000, *Baltic Astronomy*, 9, 590
- Neckel, H. & Labs, D. 1984, *Sol. Phys.*, 90, 205
- Pereira, T. M. D., Asplund, M., & Kiselman, D. 2009, *A&A*, 508, 1403
- Piskunov, N. E., Kupka, F., Ryabchikova, T. A., Weiss, W. W., & Jeffery, C. S. 1995, *A&AS*, 112, 525
- Scott, P., Asplund, M., Grevesse, N., & Sauval, A. J. 2009, *ApJ*, 691, L119
- Scott, P. C., Asplund, M., Grevesse, N., & Sauval, A. J. 2006, *A&A*, 456, 675
- Shchukina, N. & Trujillo Bueno, J. 2001, *ApJ*, 550, 970
- Shimizu, T., Nagata, S., Tsuneta, S., et al. 2008, *Sol. Phys.*, 249, 221
- Socas-Navarro, H. 2011, *A&A*, 529, A37
- Socas-Navarro, H., de la Cruz Rodríguez, J., Asensio Ramos, A., Trujillo Bueno, J., & Ruiz Cobo, B. 2014, *A&A*, *in preparation*
- Socas-Navarro, H. & Norton, A. A. 2007, *ApJ*, 660, L153
- Storey, P. J. & Zeippen, C. J. 2000, *MNRAS*, 312, 813
- Suematsu, Y., Tsuneta, S., Ichimoto, K., et al. 2008, *Sol. Phys.*, 249, 197
- Tsuneta, S., Ichimoto, K., Katsukawa, Y., et al. 2008, *Sol. Phys.*, 249, 167
- Young, L., Childs, W. J., Dinneen, T., et al. 1988, *Phys. Rev. A*, 37, 4213

**Table 1.** Spectral line data, where  $r_0$  is the Böhr radius,  $\gamma_{rad}$ ,  $\gamma_{Stark}$  and  $\gamma_{vdW}$  are the radiative, Stark and van der Waals damping enhancement constants.

<i>Element</i>	$\lambda$ (Å)	<i>Excitation(eV)</i>	$\log(gf)$	$\sigma(r_0^2)$	$\alpha$	$\gamma_{rad}$	$\gamma_{Stark}$	$\gamma_{vdW}$
O I	6300.304	0.000	-9.819	-	-	0.0	0.05	1.00
Ni I	6300.335	4.266	-2.253	-	-	2.63	0.054	1.82
Ni I	6300.355	4.266	-2.663	-	-	2.63	0.054	1.82
Sc II	6300.678	1.507	-1.89	-	-	2.30	0.050	1.30
Fe I	6301.501	3.654	-0.718	834.4	0.243	-	-	-
Fe I	6302.494	3.686	-1.160	850.2	0.239	-	-	-

**Table 2.** Inversion nodes

<i>Physical Parameter</i>	<i>Magnetic pixel</i>				<i>Non – magnetic pixel</i>	
	<i>Comp1 Cycle1</i>	<i>Cycle2</i>	<i>Comp2 Cycle1</i>	<i>Cycle2</i>	<i>Cycle1</i>	<i>Cycle2</i>
<i>Temperature</i>	3	5	2	3	3	5
<i>L.o.s. velocity</i>	1	3	1	2	2	3
<i>Microturbulence</i>	1	1	0	0	0	0
$B_{long}$	0	0	1	2	0	0
$B_x$	0	0	1	2	0	0
$B_y$	0	0	1	2	0	0
<i>Filling factor</i>	0	0	1	1	0	0